Renewable and Sustainable Energy Reviews 34 (2014) 517–524

Contents lists available at ScienceDirect

Renewable and Sustainable Energy Reviews

journal homepage: www.elsevier.com/locate/rser

Design and analysis of high-power/high-torque density dual excitation switched-flux machine for traction drive in HEVs

Erwan Sulaiman [a,b,*], Takashi Kosaka [b], Nobuyuki Matsui [b]

[a] Department of Electrical Power Engineering, UTHM, Johor, Malaysia
[b] Department of Electrical & Comp. Sci. Engg, NIT, Nagoya, Japan

A R T I C L E I N F O

Article history:
Received 23 October 2012
Received in revised form
19 January 2014
Accepted 13 March 2014
Available online 3 April 2014

Keywords:
Dual excitation switched-flux (DESF) motor
Permanent magnet (PM)
Field-excitation (FE) Coil
Hybrid electric-vehicle (HEV)

A B S T R A C T

This paper presents design viability studies and investigations of dual excitation switched-flux (DESF) motor as an applicant for traction drives in hybrid electric vehicles (HEVs). First of all, the main structure, the fundamental principle of operation and the design notion of the recommended DESF motor are discussed. Then, under certain limitations, specifications and performances of conventional interior permanent magnet synchronous (IPMS) motor, the preliminary performances of the recommended DESF motor are evaluated based on two-dimensional Finite Element Analysis (FEA). Since the initial performances fail to attain the target torque and power, design optimization based on deterministic approach of several DEFS motor parameters is applied in an attempt to attain the target performances. After a few cycles of design optimization, the improved DEFS motor has achieved the target power and torque of 123 kW and 333 Nm, respectively. In addition, due to definite advantage of robust rotor structure of DESF motor, rotor mechanical stress prediction at highest speed of 12,400 r/min is much lower than the mechanical stress in conventional IPMS motor. In conclusion, the final design DESF motor has the maximum torque of 11.97 Nm/kg and power density of 5.83 kW/kg, which is approximately 26% and 66% more than the torque and power density in existing IPMS motor.

Contents

1. Introduction

Many alternative energy resources have been used for hybrid vehicles to substitute the exhausted supply of petroleum worldwide. Fossil fuel in the vehicles is not used due to its destructive environmental effects. Battery, fuel cell (FC), super capacitors (SC) and photovoltaic cell i.e. solar are studied for vehicle use. These sources of renewable energies can be well-designed for hybrid electric vehicle (HEV) for next invention of transportation. Literature reviews have explained many issues, disputes and problems sustainable next generation hybrid vehicle [1]. Additionally, some researchers have discussed modeling of backup energy systems (Diesel Generator,

* Corresponding author at: Department of Electrical Power Engineering, UTHM, Johor, Malaysia.
E-mail address: erwan@uthm.edu.my (E. Sulaiman).

http://dx.doi.org/10.1016/j.rser.2014.03.030
1364-0321/

Ultra-capacitor, Battery, and Fuel Cell), hybrid energy resources (Photovoltaic systems), power conditioning components (Battery chargers, Buck/Boost converters) and other methods to manage the energy flow in detail [2].

In electrical machines, electric motors are used to transform one form of energy into another (electrical energy to mechanical energy). Electrical motor is categorized into two main classes that are alternating current (AC) motor and direct current (DC) motor and then further classified as shown in Fig. 1. Sensorless controlled Induction motor drives have various applications when dealing with efficiency improvement and energy savings of electric vehicles, compressors, high performance machine tools, fans, etc [3].

Dual excited machine (DEM) consists of field excitation (FE) Coil and permanent magnet (PM), has various unique characteristics that can be beneficial for HEV drive system. Generally, DEM can be classified into four types based on the placement of PM and FE Coil such as (i) the PM is in the rotor while the FE Coil is in the stator [4] (ii) both FE Coil and PM are placed at rotor side [5–7] (iii) the PM is in the rotor while the FE Coil is in the machine end [8,9], and (iv) both PM and FE Coil are placed in the stator [10–12]. All DEMs where PM is placed at the rotor can be categorized as "hybrid rotor-PM with FE Coil machines" whiles the machine having PM and FE Coil located at stator can be referred as "hybrid stator-PM with FE Coil machines". Based on its principles of operation, in which flux sources are generated in stator side and moved into the rotor, the fourth machine is also known as "Dual excitation switched-flux motor" (DESF) motor which obtained more popularity in recent years [7,13]. In DESF motor, all major parts are placed on stator. Thus, it has the following advantages (i) a simple cooling mechanism can be used because all major heats are accumulated in stator part, compared with a complex water jacket system used in IPMS motor for Lexus RX400h, (ii) robust rotor structure which makes it more appropriate to be used in high-speed drive applications and (iii) the extra FE Coil that can be employed to control flux with variable flux capabilities.

For high speed applications, different arrangements of rotor pole and stator slot for DESF motor have been developed. For example, 12S-10P DESF motor has been proposed such as in [14,15] whereas the machine in [15] has insufficient power and torque production at high current density condition. This is because of inadequate width of stator yoke between armature coil slots and FE Coil that creates problem of negative torque production and magnetic saturation. However, the machine in [16] having separated C-type stator core and PM makes it complex to manufacture, and the optimization techniques is not so far applied to the design for HEV applications. The authors have been suggested 6S-5P DESF motor to decrease the supply frequency of inverter. Although through that proposed machine, the target performances are achieved but the problem of unbalanced pulling magnetic force due to odd number of poles made the machine impractical [16]. Additionally, 6–8P machines have been proposed by some researchers but high torque ripples and back-emf waveforms are the main problems which are typical concerns for this type of 8 Pole machine [17,18].

FSM has the advantages of high output torque, low cost power converter and high speed, easily controllable; particularly the relative lower intensity vibration and acoustic noise [19,20]. Because of the above mentioned advantages, FSM catches the attention of industries for applications where huge amount of torque is required, e.g. HEV propulsion systems [21]. The electromagnetic performance of the FSPM machine was analyzed and its design constraints were optimized [22,23]. The other design parameter, for example the influence of the iron loss [24] and the end-effect [25] were also examined. A number of PM motors and control approaches with differing degrees of Fault-Tolerant (FT) potential have emerged in the literature [26–29]. A latest technique which is based on control level instead of motor design level to minimize the torque ripple of 12-slot/10-pole FSPM motor is investigated [30]. The FT potential of flux switching machines has been mentioned [31].

To accomplish the target performances for HEV applications, design viability and optimization studies are presented for 12S-10P DESF motor in this paper. Fig. 2 illustrates the cross-sectional view of the main machine part of the initial DESF motor. The motor is made up of 12 FE Coils and12 PMs spread uniformly in the middle of each armature coil whereas the three-phase armature coils are housed in the 12 slots for each 1/4 stator body periodically. The PMs and FE Coils produce six north poles interspersed between six south poles in this motor. The flux paths produced by both mmf of FE Coil and PM under no load condition are shown in Fig. 3. The term, "flux switching", is created based on the changes in polarity of each flux in each stator tooth, depending on the rotor position. The fluxes produced by PM and FE Coil link with the armature coil flux alternately with the rotation of rotor. The flux linkage of the armature coil has one periodic cycle as the rotor rotates through 1/10 of a revolution and consequently, the back-emf induced in the armature coil becomes ten times of the mechanical rotational frequency.

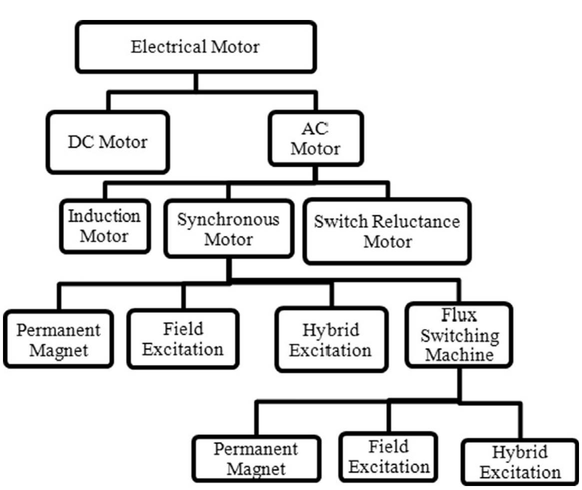


Fig. 1. Classification of electrical motors.

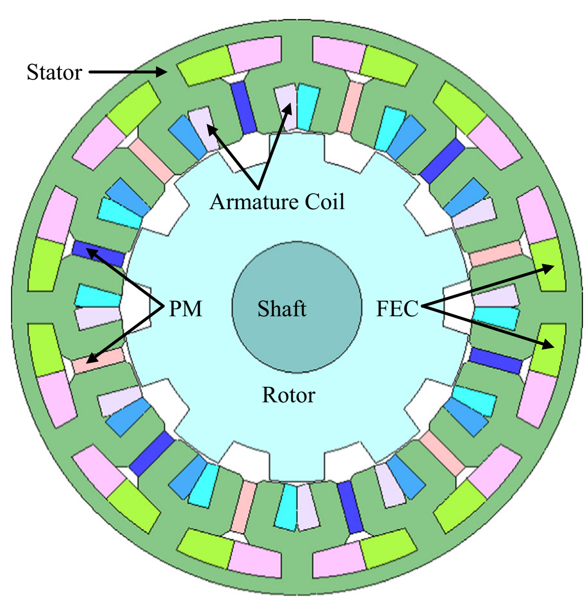


Fig. 2. 12S-10P DESF motor.

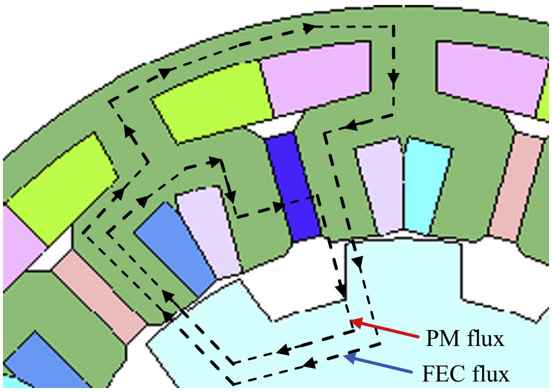


Fig. 3. Direction of flux of PM and FE Coil in 12S-10P DESF motor.

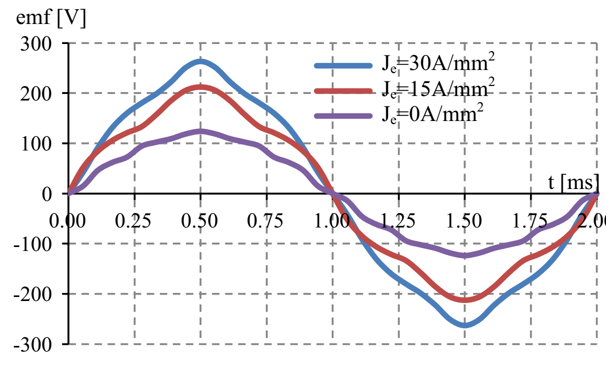


Fig. 4. Back-emf at 3000 r/min.

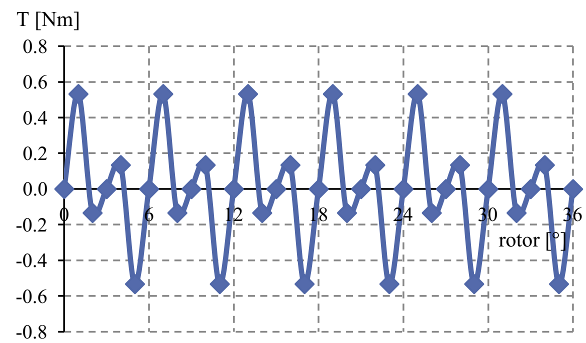


Fig. 5. Cogging torque of the original design DESF motor.

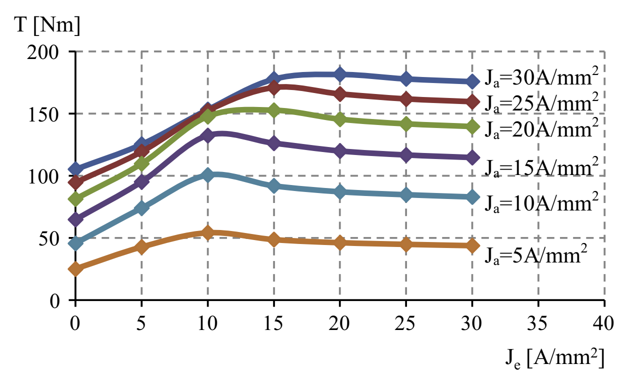


Fig. 6. Torque versus J_e at various J_a.

Table 1
DESF motor design specifications and limitations.

Items	IPMS motor	DESF motor
Maximum DC voltage (V)	650	650
Maximum current (A_{rms})	360	360
Maximum J_a (A_{rms}/mm^2)[a]	31	30
Maximum J_e (A/mm^2)[b]	NA	30
Stator diameter (mm)	264	264
Machine length (mm)	70	70
Diameter of shaft (mm)	60	60
Air-gap (mm)	0.8	0.8
PM volume (kg)	1.1	1.1
Max. speed (r/min)	12,400	12,400
Max. torque (Nm)	333	333
Reduction-gear (RG) ratio	2.478	2.478
Max. axle torque via RG (Nm)	825	825
Max. power (kW)	123	> 123
Power density (kW/kg)	3.5	> 3.5

J_a is current density in armature coil.
J_e is current density in FE Coil.

2. Design conditions, limitations and requirements for HEV applications

The design conditions, limitations and requirements of the suggested DESF motor for HEV applications are analogous with IPMS motor for Lexus RX400h listed in Table 1 [32]. FE Coil current density, J_e and Armature coil current density, J_a must have values of 30 A/mm^2 and 30 A_{rms}/mm^2, respectively. The target torque of 333 Nm with reduction gear ratio of 2.476 is set, hence, realizing the maximum axle torque via reduction gear of 825 Nm. The PM weight in DESF motor is 1.1 kg similar with PM weight in IPMS motor. The target power is set to be more than 123 kW and the maximum operating speed is set to 12,400 rev/min. The proposed DESF motor has simple configuration with concentrated winding in all coils; therefore weight less than 35 kg is set for the design of target motor to achieve maximum power density of more than 35 kg. The electrical limitations related with the inverter are set as maximum 650 V DC bus voltage and maximum 360 A inverter current. Commercial FEA package, JMAG-Studio ver.12.0, released by Japanese Research Institute (JRI) is used as 2D FEA solver in this design.

3. Initial performances of the proposed DESF motor based on 2D FEA

Figs. 4 and 5 illustrate the initial performances such as back-emf and cogging torque of the proposed DESF motor under no load condition. The amplitude of induced voltage generated from the flux of PM only is 123.59 V depicted in Fig. 4. Less amount of cogging torque approximately 1.07 Nm peak-to-peak is produced due to slightly sinusoidal back-emf. However, the induced voltage is distorted to some extent at J_e = 15 A/mm^2 and the amplitude is raised to 262.19 V which is more than twice of that at no FE Coil current. The reason is the field intensification effect by the additional FE Coil. The performances of machine at maximum J_e and J_a are examined for load analysis. At base speed of 5731.4 r/min, the power and torque obtained are 105.6 kW and 175.9 Nm, respectively, which is below the desired value. To inspect this problem, the torque versus J_e at different values of J_a is plotted as shown in Fig. 6. It is clear that the torque is increased up to certain value of J_e and then started decreasing when higher J_e is applied. For instance, the maximum torque of 181.65 Nm is achieved at J_a of 30 A_{rms}/mm^2, when J_e is set to 20 A/mm^2. On the other hand, the torque starts to decrease when J_e is set greater than this value. The maximum torque obtained is 152.71 Nm and 170.93 Nm for J_a of 20 A_{rms}/mm^2 and 25 A_{rms}/mm^2, when J_e is set to 15 A/mm^2.

The torque also begins to decrease when J_e is set higher than this value. Similarly, the same phenomenon occurs at the condition of J_a of 5 A_{rms}/mm^2, 10 A_{rms}/mm^2 and 15 A_{rms}/mm^2 where the torque begins to decrease when J_e is set higher than 10 A/mm^2.

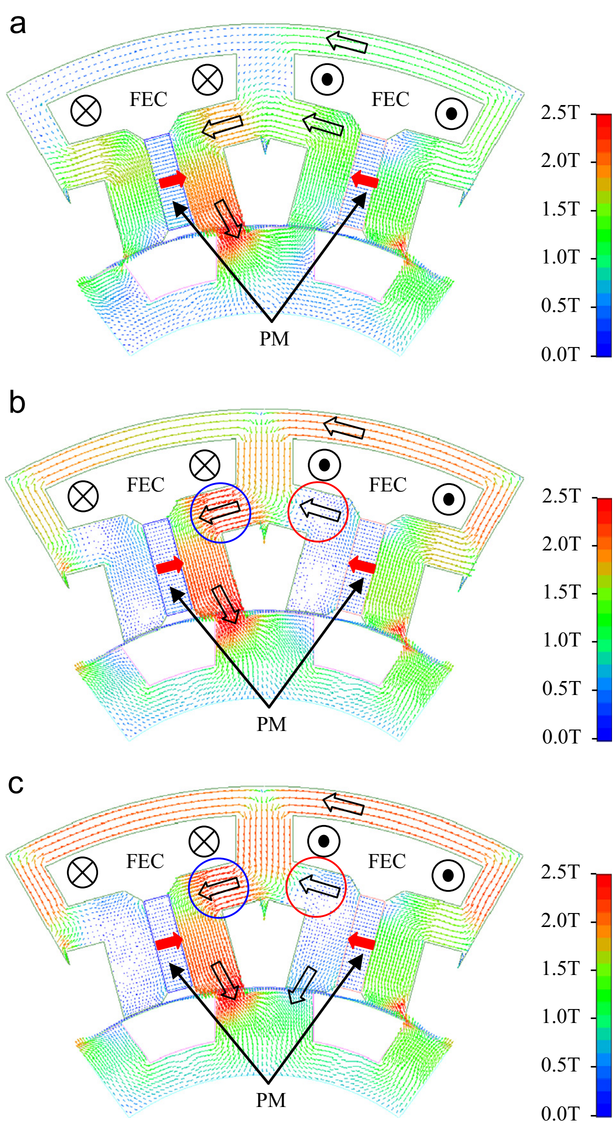


Fig. 7. Flux vector diagram of various J_e at maximum J_a of 30 A_{rms}/mm^2 (a) J_e = 10 A/mm^2, T = 153.4 Nm (b) J_e = 20 A/mm^2, T_{max} = 181.7 Nm and (c) J_e = 30 A/mm^2, T = 175.9 Nm. (For interpretation of the references to color in this figure the reader is referred to the web version of this article.)

For further investigation and explanation of this phenomenon, three situations such as (i) after maximum torque (ii) before maximum torque and (iii) at maximum torque, are studied for flux density distribution. For instance, at maximum J_a of 30 A_{rms}/mm^2, flux distribution at J_e of 10 A/mm^2, 20 A/mm^2 and 30 A/mm^2 are investigated as illustrated in Fig. 7. It can be observed that for low value of J_e such that 10 A/mm^2, the flux can easily follow the paths as shown in Fig. 7(a). However, when J_e is set to 20 A/mm^2, the flux flow to the left part starts to saturate between FE Coil lower slot and armature coil upper slot marked in blue circle as revealed in Fig. 7(b). In this case, the flux from FE Coil and PM canceled the effect of each other as can be seen in red circle which results in lowering the torque production. Consequently, for maximum Je of 30 A/mm^2, where large amount of flux is generated by FE Coil, the flux flow to the left side is completely saturated between FE Coil lower slot and armature coil upper slot marked in blue circle. Therefore, much higher flux from the stator outer yoke passes the FE Coil pitch move towards the PM in the right side. This flux also canceled the PM flux and some of the flux is forced to flow into the rotor side producing much negative torque as shown in Fig. 7(c), hence reducing the torque production. To overcome this problem, suitable length is investigated between FE Coil lower slot and armature coil upper slot to avoid flux saturation.

4. Design methodology for improvements

The structure of air gap and armature coil slot between the internal and external PM are redesigned to make a simple machine, in order that design free parameters of D_1–D_{10} can be identified as illustrated in Fig. 8. The initial step is taken by changing the rotor parameters, D_1–D_3 whilst keeping D_4–D_{10} as constant. As the torque increases by increasing rotor radius, D_1 is treated initially because it is the only leading parameter which can improve the torque. In this circumstance, D_4, D_6 and D_8—D_{10} are simply transferred to the new position by following the movement of D_1, while D_5 and D_7 are kept constant. The value of D_1 for maximum performance is selected and then to determine the maximum performance from the combined effect of D_2 and D_3, both rotor pole depth D_3 and rotor pole width D_2 are varied. By keeping the other parameters constant, the second step is taken by varying the FE Coil slot parameters D_4–D_6. Then, by using the arrangement of D_4–D_6 that reveal the maximum performance at the second step, the third step is taken by changing the armature coil slot parameters D_7 and D_8 while keeping other parameters constant. The required armature coil slot area, S_a is determined by changing armature coil depth, D_7 and armature coil width, D_8 to house natural number of turns, N_a for armature coil. Moreover, to make sure that the PM is not demagnetized at high temperatures

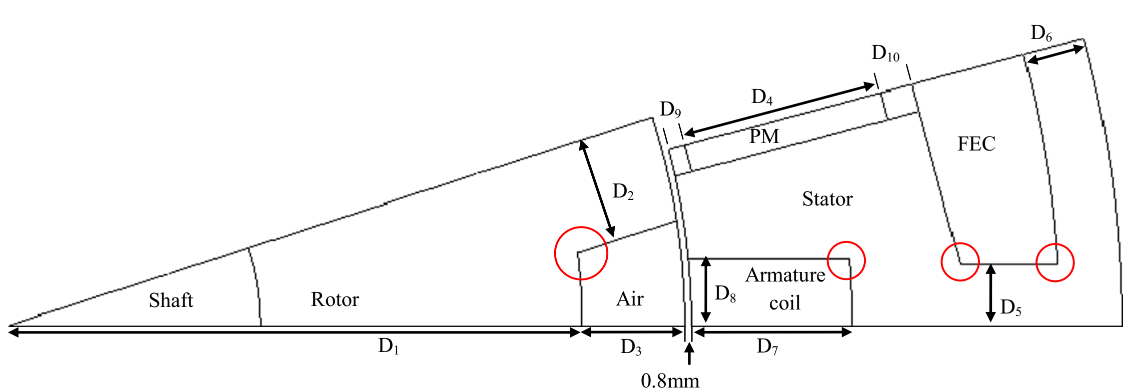


Fig. 8. Design parameter defined as D_1–D_{10}.

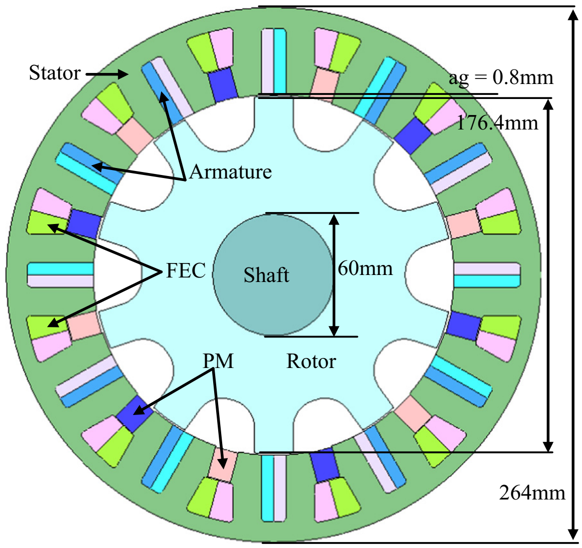


Fig. 9. Final design DESF motor.

Table 2
Initial and final design parameters.

	Details PM volume (kg)	Initial 1.1	Final 1.1
D_1	Rotor radius (mm)	80.2	88.2
D_2	Rotor pole width (mm)	12.5	9.5
D_3	Rotor pole depth (mm)	12.2	23.2
D_4	Permanent magnet height (mm)	24.0	15.0
D_5	FEC slot pitch (mm)	7.4	20.0
D_6	Thickness of stator outer core (mm)	7.4	8.0
D_7	Width of armature coil (mm)	8.0	6.0
D_8	Depth of Armature coil (mm)	19.1	32.71
D_9	Distance between PM and air gap (mm)	2.0	0.5
D_{10}	Distance between PM and FE Coil (mm)	4.0	0.5
N_a	Armature coil turns	7	9
T	Torque (Nm)	175.86	334.5
N	Speed (r/min)	5731.4	3701.2
P	Power (kW)	105.55	129.6
pf	Power factor	0.368	0.452

such as 180 °C, D_9 and D_{10} are adjusted for same PM volume. To attain the target performances, the method of changing D_1–D_{10} is treated repeatedly.

Under maximum J_a and J_e, all design parameters are modified having constant air gap length of 0.8 mm. In addition to the final design, the corners circled in Fig. 8 are proposed as a curve to make sure that all flux at the edge of the design flow more easily, therefore enhances the performance of the machine. The curve design for the rotor inner pole not only increased the flux flow but also increases the rotor mechanical strength of the machine; making it more robust to work in high speed applications. Finally, after few cycle of optimization, the machine fulfilled the target requirements and performances for HEV applications. Fig. 9 depicts the cross sectional views of the final design DESF motor, whereas specifications of final design parameters are listed in Table 2.

The major distinctions between the initial and the final design DESF motor are (i) the armature coil breadth of the final design is not as much of the initial design, but results in more number of turns due to high armature coil depth, (ii) the final design has longer radius as compare to initial design which provides additional torque as had been anticipated (iii) the flux saturation problem is solved when no gap is left between FE Coil lower slot and armature coil upper slot in final design (iv) the thickness of final design stator core is greater than the initial design to permit more flux to flow easily, (v) the FE Coil slot area is decreased about 40% from the initial design to cover some volume of stator yoke used for armature coil, (vi) the final design has a stator yoke with a straight "I shape" that allows the flux to flow into the rotor more smoothly and (vii) the final design has high PM width with less PM depth to maintain the same PM volume of 1.1 kg.

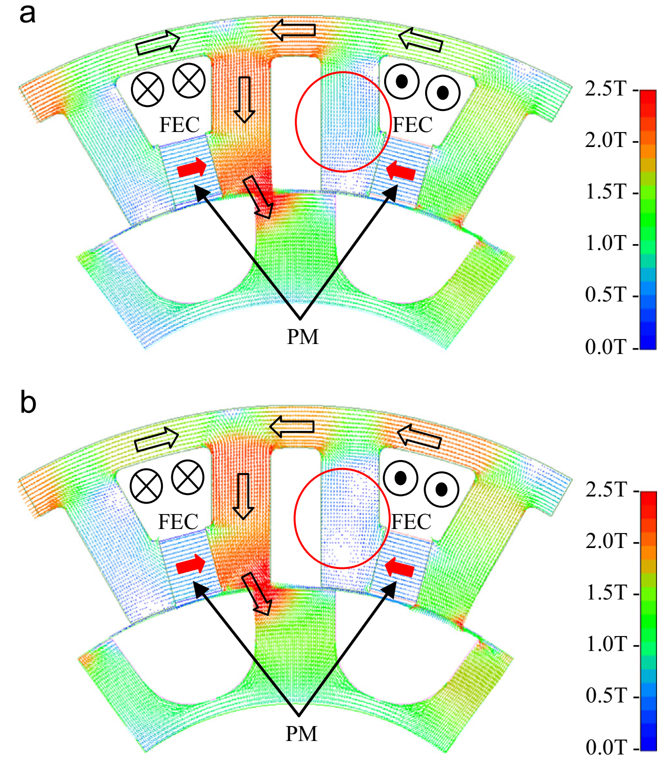


Fig. 10. Flux vector diagram of various J_e at maximum J_a of 30 A_{rms}/mm^2 (a) J_e=20 A/mm^2, T=280.4 Nm and (b) J_e=30 A/mm^2, T=334.4 Nm. (For interpretation of the references to color in this figure the reader is referred to the web version of this article.)

The problem of magnetic saturation caused by higher FE Coil is resolved, as the gap between FE Coil lower slot and armature coil upper slot illustrated in the final design DESF motor is considered negligible. Fig. 10 illustrates the flux distribution of the final design DESF motor for J_e of 20 A/mm^2 and 30 A/mm^2 with maximum J_a of 30 A_{rms}/mm^2. The red circle in Fig. 10(a) and (b) represents the difference of flux interaction between PM and FE Coil without negative torque production. Thus, the same amount of torque for both current density conditions is maintained by the improved design and permits to extract higher power factor.

5. Results and performances of the final design DESF motor

5.1. Flux linkage under no load condition

The investigation of open circuit field distribution based on 2D FEA for PM and FE Coil of the final design DESF motor is illustrated in Fig. 11. Fig. 11(a) shows the flux path due to mmf of PM only, whereas Fig. 11(b) represents the combination of flux lines for both PM and FE Coil at maximum FE Coil density, J_e of 30 A/mm^2. From Fig. 11(a), it is clear that almost 100% flux of PM flow in the stator iron around the FE Coil. This results negligible cogging torque and almost no back-emf at no load condition under the maximum speed operation, which makes it easy to provide

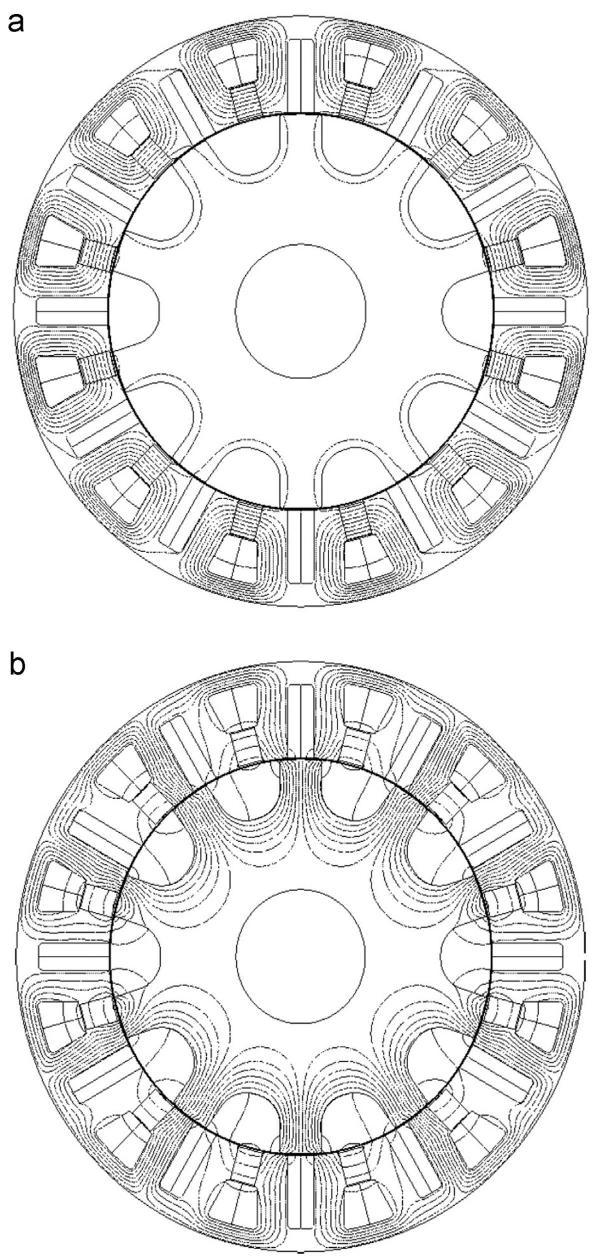


Fig. 11. Flux path of the final design DESF motor at no load condition (a) PM only (b) PM and maximum FE Coil current density of 30 A/mm^2.

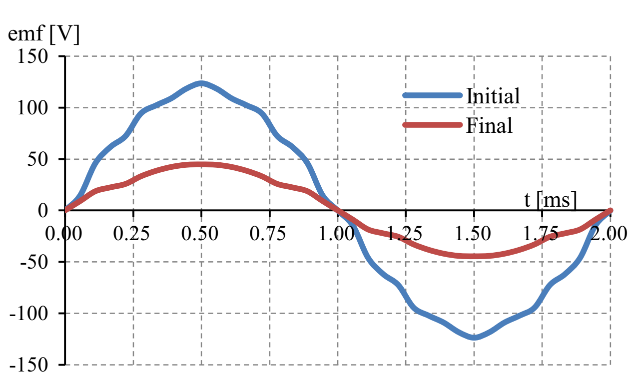


Fig. 12. Back-emf.

protection for switching devices while the inverter is in off state due to some faults. On the contrary, a large amount of fluxes follow the path to the rotor side due to field strengthening excitation thus generates maximum torque with the help of dual excitation as shown in Fig. 11(b).

Additionally, Figs. 12 and 13 depict the evaluation between cogging torque and back-emf of the initial and final design at speed of 3000 r/min. It is obvious that, final design has more sinusoidal back emf as compared to initial design but approximately less by 36%. The final design DESF motor has reduced cogging torque of more than 50% judged against initial design.

5.2. Torque and power factor versus J_e characteristics

The torque and power factor for different J_e values are plotted in Figs. 14 and 15, respectively. From the graph, it is clear that higher J_a values will enhance the torque but the power factor gets reduced. To equilibrate this condition, J_e is increased to certain value such that the power factor can be improved and remain

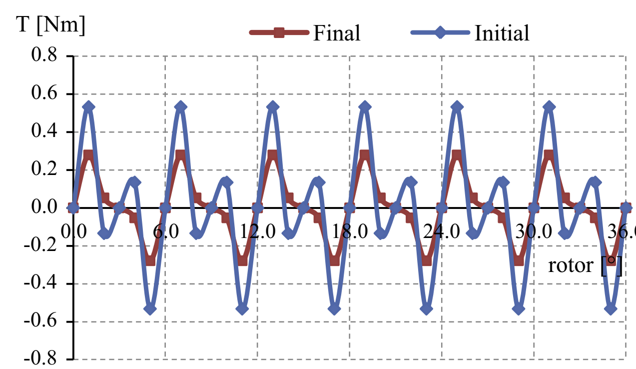


Fig. 13. Cogging torque.

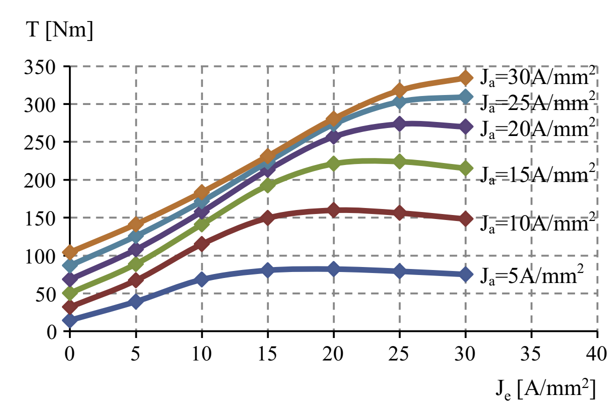


Fig. 14. Torque versus J_e.

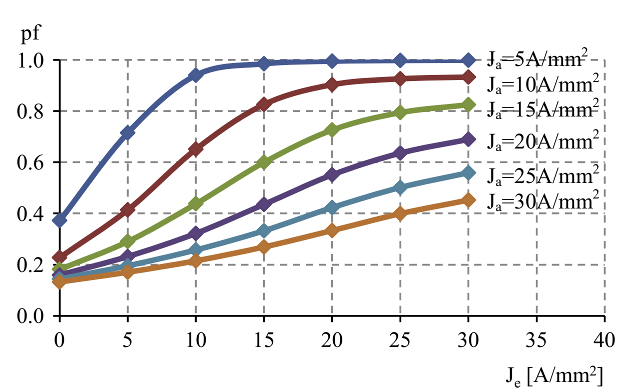


Fig. 15. Power factor versus J_e.

constant although J_a has very high value. The graphs obviously illustrate that maximum torque of 334.42 Nm is achieved when both J_a and J_e are set to 30 A/mm^2 as their maximum value with the power factor of 0.4519. On the other hand, for low value J_a less than 15 A_{rms}/mm^2, the torque is reduced to some extent with the increasing of J_e value more than 20 A/mm^2. Excessive FEC flux occurs in this condition that produces negative torque and affecting the performances of machine, analogous with the original DESF motor discussed earlier. Both torque and power factor are compared for different values of J_e under maximum J_a for the initial and final design DESF motor as illustrated in Fig. 16. The power factor and torque of the final design DESF motor improved approximately 23% and 50%, respectively when compared with the original design.

5.3. Torque and power versus speed characteristics

Torque speed characteristics of the DESF motor and IPMS motor are illustrated in Fig. 17. The maximum torque attained by IPMS motor is 333 Nm and final design DESF motor is 334.42 Nm. In high speed region, DESF motor produced much higher torque and has better torque condition. Meanwhile, Fig. 18 shows the power versus speed characteristics of the IPMS motor and DESF motor. From the graph, (i) at maximum torque, the power accomplished by IPMS motor and the final design DESF motor is 72.09 kW and 129.58, at the speed of about 2100 r/min and 3701 r/min (ii) the maximum power achieved is 123.08 kW for IPMS motor and 162.79 kW for DESF motor (iii) at normal driving mode the IPMS motor and the DESF motor has the average power of 113.7 kW and 133.7 kW, having speed of 3000–6000 r/min, which shows that in frequent driving condition, the performance of DESF motor is better than IPMS motor.

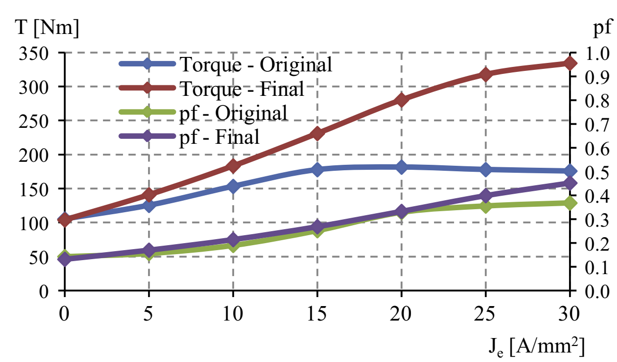


Fig. 16. Torque and power factor versus J_e.

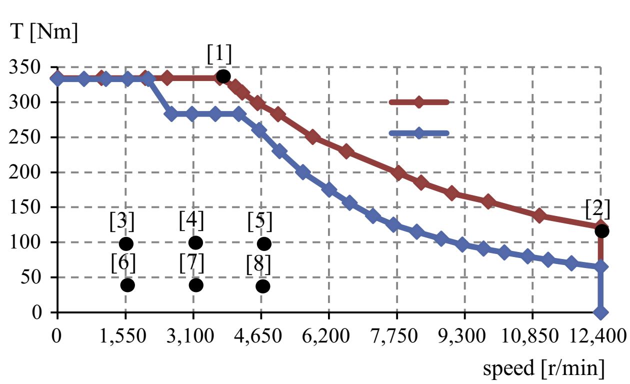


Fig. 17. Torque versus speed characteristics.

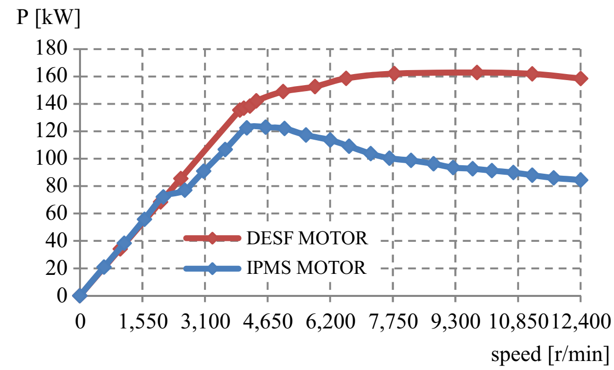


Fig. 18. Power versus speed characteristics.

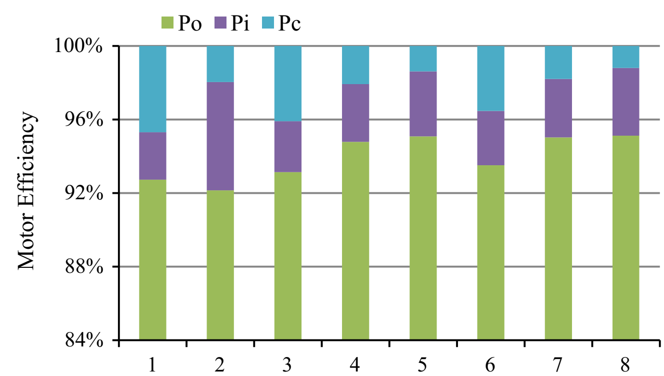


Fig. 19. Motor efficiency.

The total weight of the final design DESF motor including armature coil, FE Coil, stator iron, PM, rotor iron, and estimation of both coil ends is 29.29 kg and 35 kg for IPMS motor, which has 16.2% difference such that the weight of final design DESF motor is reduced. Thus, for HEV applications the maximum power density and maximum torque density achieved are 5.57 kW/kg and 11.43 Nm/kg, respectively, much higher than the target requirements. The maximum torque and power density of DESF MOTOR are raised in the order of 20.0% and 36.9%, judged against existing IPMS motor having 9.499 Nm/kg and 3.52 kW/kg.

5.4. Motor losses and efficiency

The losses and efficiency of motor are measured by taking into consideration the copper losses in armature coil and FE Coil, and the iron losses in all laminated cores. Under light load driving condition, the losses and motor efficiency of the final design DESF motor at maximum power, maximum torque, and frequent operating point noted as No. 1–No. 8 in Fig. 17 are shown in Fig. 19. At high torque operating points No. 1, due to high copper losses the efficiency is decreased to some extent while at high-speed operating point No. 2, due to high iron losses the motor efficiency is decreased. Moreover, under light load condition at frequent driving operation No. 3–No. 8, the proposed machine attains comparatively high efficiency of 93% and above.

5.5. Rotor mechanical strength

2D FEA is used to predict the mechanical stress of rotor design, determined by centrifugal force analysis as illustrated in Fig. 20. At a speed of 12,400 r/min, the original and final designs have achieved the maximum stress of 46 MPa and 28 MPa, respectively which is much lesser than permissible maximum stress of 300 MPa in conservative electromagnetic steel. This is one of the

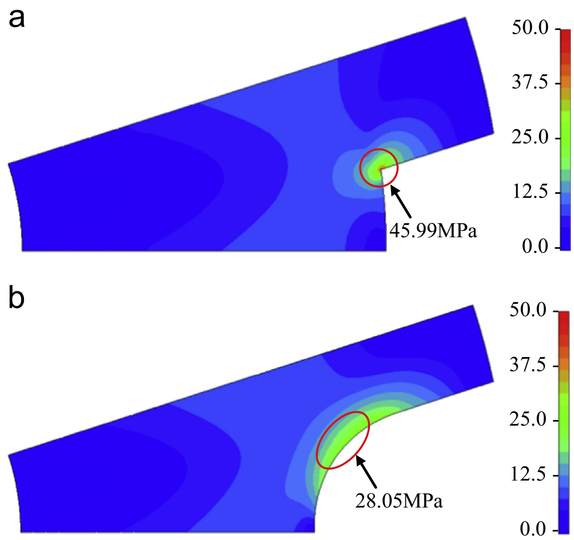


Fig. 20. Main stress distributions of rotor at 12,400 r/min (a) initial design and (b) final design.

great advantages of the final design DESF motor that make its appropriate use in high-speed appliances as compared to conventional IPMS motor.

6. Conclusion

Design viability studies and performance investigation of 12S-10P DESF motor for traction drive in the target HEV is presented in this paper. The design modification is illustrated and explained. The final design DESF motor attained the target performances. Furthermore, in high-speed region, the rotor mechanical stress investigated is satisfactory for the operation of machine. In general, torque of DESF motor has better characteristics than IPMS motor at high speed. Finally for LEXUS RX400h, the power density of the final design DESF motor is improved more than one third judged against existing IPMS motor.

The advantages of DESF motor at a glance are significantly lower operating costs when compared with IPMS motor. DESF motor has comparatively reduced weight than IPMS motor, thus less material usage will decrease the cost and enough free space will compact the size of HEV in future. With all the analytical investigations, the proposed DESF motor will definitely give the best result when tested with a prototype model as compared with the previous work did by many researchers. As a conclusion, the aim of this research to obtain maximum performances for HEV applications is effectively accomplished.

References

[1] Hannan MA, Azidin FA, Mohamed A. Hybrid electric vehicles and their challenges: a review. Renew Sustain Energy Rev 2014;29:135–50.
[2] Bajpai P, Dash V. Hybrid renewable energy systems for power generation in stand-alone applications: a review. Renew Sustain Energy Rev 2012;16 (5):2926–39.
[3] Alsofyani IM, Idris NRN. A review on sensorless techniques for sustainable reliability and efficient variable frequency drives of induction motors. Renew Sustain Energy Rev 2013;24:111–21.
[4] Tapia JA, Leonardi F, Lipo TA. Consequent-pole permanent-magnet machine with extended field-weakening capability. IEEE Trans Ind Appl 2003;39 (6):1704–9.
[5] Xiaogang L, Lipo TA. A synchronous/permanent magnet hybrid AC machine. IEEE Trans Energy Convers 2000;15(2):203–10.
[6] Naoe N Fukami T, Trial production of a hybrid excitation type synchronous machine. In: Proceedings of IEEE international electric machines and drives conference, MIT, USA. 20 June; 2001. p. 545–547.
[7] Fodorean D, Djerdir A, Viorel IA, Miraoui A. A double excited synchronous machine for direct drive application-design and prototype tests. IEEE Trans Energy Convers 2007;22(3):656–65.
[8] Kosaka T Matsui N. Hybrid excitation machines with powdered iron core for electrical traction drive applications. In: Proceedings of the international conference on electrical machines and systems. Wuhan, China, 17–20 October; 2008. p. 2974–2979.
[9] Kosaka T, Sridharbabu M, Yamamoto M, Matsui N. Design studies of hybrid excitation motor for main spindle drive in machine tools. IEEE Trans Ind Electron 2010;57(11):3807–13.
[10] Chen Z, Sun Y Yan Y. Static characteristics of a novel hybrid excitation doubly salient machine. In: Proceedings of the eight international conference on electrical machines and systems. Nanjing, China. 27–29 September; 2005, p. 718–721.
[11] Chau KT, Jiang JZ, Yong W. A novel stator doubly fed doubly salient permanent magnet brushless machine. IEEE TransMagn 2003;39(5):3001–3.
[12] Amara Y, Vido L, Gabsi M, Hoang E, Ben Ahmed AH, Lecrivain M. Hybrid excitation synchronous machines: energy-efficient solution for vehicles propulsion. IEEE Trans Veh Technol 2009;58(5):2137–49.
[13] Tapia JA, Leonardi F, Lipo TA. Consequent-pole permanent magnet machine with extended field-weakening capability. IEEE Trans Ind Electron 2003;39 (6):1704–9.
[14] Wei H, Ming C, Gan Z. A novel hybrid excitation flux-switching motor for hybrid vehicles. IEEE Trans Magn 2009;45(10):4728–31.
[15] Hoang E, Lecrivain M and Gabsi M. A new structure of a switching flux synchronous polyphased machine with hybrid excitation. In: Proceedings of the european conference on power electronics and applications. Aalborg, Denmark. 2–5 September; 2007, p. 1–8.
[16] Sulaiman E, Kosaka T, Matsui N. Design optimization and performance of a novel 6-slot 5-pole PMFSM with hybrid excitation for hybrid electric vehicle. IEEJ Trans Ind Appl 2011;132(2, Sec. D):211–8.
[17] Zulu A, Mecrow BC, Armstrong M. A wound-field three-phase flux-switching synchronous motor with all excitation sources on the stator. IEEE Trans Ind Appl 2010;46(6):2363–71.
[18] Sulaiman E, Kosaka T, Matsui N. High power density design of 6slot-8pole hybrid excitation flux switching machine for hybrid electric vehicle. IEEE Trans Magn 2011;47(10):4453–6.
[19] Bangura. JF. Design of high-power density and relatively high efficiency flux switching motor. IEEE Trans Energy Convers 2006:416–25.
[20] Pollock C, Brackley M, Comparison of the acoustic noise of a flux switching and a switched reluctance drive. In: Proceedings of the industry applications conference. 36th IAS annual meeting. Conference record; 2001.
[21] Y Tang, TE Motoasca, JJH Paulides, EA Lomonova. Comparison of flux-switching machines and permanent magnet synchronous machines in an in-wheel traction application. In: Proceedings of EVER, Monco 2011, p. 1–10.
[22] Zhu ZQ, Pang Y, Howe D, Iwasaki S, Deodhar R, Pride A. Analysis Of electromagnetic performance of flux-switching pm machine by non-linear adaptive lumped parameter magnetic circuit model. IEEE Trans Magn 2005;41 (11):4277–87.
[23] Chen JT, Zhu ZQ. Winding configurations and optimal and rotor pole combination of flux-switching pm brushless ac machines. IEEE Trans Energy Convers 2010;25(2):293–302.
[24] Y Pang, ZQ Zhu, D Howe, S Iwasaki, R Deodhar, A Pride. Investigation of iron loss in flux-switching pm machines. In: Proceedings of IET power electronics, machines & drives, UK; 2–4 April; 2008, p. 460–464.
[25] Zhu ZQ, Pang Y, Hua W, Cheng M, Howe D. Investigation of end-effect in pm brushless machines having magnets in the stator. J Appl Phys 2006;99(8):1–3 (08R319).
[26] Mecrow BC, Jack AG, Atkinson DJ, Green SR, Atkinson GJ, King A, Green B. Design and testing of a four-phase fault-tolerant permanent-magnet machine for an engine fuel pump. IEEE Trans Energy Convers 2004;19(4):671–8.
[27] Sun Z, Wang J, Jewell G, Howe D. Enhanced optimal torque control of fault-tolerant permanent magnet machines under flux weakening operations. IEEE Trans Ind Electron 2010;57(1):344–53.
[28] EL-Refaie AM. Fractional-slot concentrated-windings synchronous permanent magnet machines: opportunities and challenges. IEEE Trans Ind Electron 2010;57(1):107–21.
[29] Dwari S, Parsa L. Fault-tolerant control of five-phase permanent-magnet motors with trapezoidal back emf. IEEE Trans Ind Appl 2011;58(2):476–85.
[30] Jia H, Cheng M, Hua W, Zhao W, Li W. Torque ripple suppression in flux-switching pm motor by harmonic current injection based on voltage space-vector modulation. IEEE Trans Magn 2010;46(6):1527–30.
[31] Thomas S, Zhu ZQ, Owen RL, Jewell GW, Howe D. Multi-phase flux-switching permanent magnet brushless machine for aerospace application. IEEE Trans Ind Appl 2009;45(6):1971–81.
[32] Kamiya M. Development of traction drive motors for the Toyota hybrid systems. IEEJ Trans Ind Appl 2006;126(4, Sec. D):473–9.